Ultrafast quantum interferometry with energy-time entangled photons

Jean-Philippe W. MacLean,[1,2,*] John M. Donohue,[1,2,3,†] and Kevin J. Resch[1,2]
[1]Institute for Quantum Computing, University of Waterloo, Waterloo, Ontario, Canada, N2L 3G1
[2]Department of Physics & Astronomy, University of Waterloo, Waterloo, Ontario, Canada, N2L 3G1
[3]Integrated Quantum Optics, Applied Physics, Paderborn University, 33098 Paderborn, Germany

(Received 12 March 2018; published 13 June 2018)

Many quantum advantages in metrology and communication arise from interferometric phenomena. Such phenomena can occur on ultrafast timescales, particularly when energy-time entangled photons are employed. These have been relatively unexplored as their observation necessitates time resolution much shorter than conventional photon counters. Integrating nonlinear optical gating with conventional photon counters can overcome this limitation and enable subpicosecond time resolution. Here, using this technique and a Franson interferometer, we demonstrate high-visibility quantum interference with two entangled photons, where the one- and two-photon coherence times are both subpicosecond. We directly observe the spectral and temporal interference patterns, measure a visibility in the two-photon coincidence rate of $(85.3 \pm 0.4)\%$, and report a Clauser–Horne–Shimony–Holt–Bell parameter of 2.42 ± 0.02, violating the local-hidden variable bound by 21 standard deviations. The demonstration of energy-time entanglement with ultrafast interferometry provides opportunities for examining and exploiting entanglement in previously inaccessible regimes.

DOI: 10.1103/PhysRevA.97.063826

Interferometry based on entangled quantum states is essential for enhanced metrology and quantum communication. Quantum correlations can enable interferometric measurements with improved sensitivity [1] and resolution [2], and quantum advantages have been found for interferometric applications involving optical coherence tomography [3], precise measurements of optical properties [4,5], and the detection of gravitational waves [6]. In laser physics, the development of ultrafast light sources has led to innovations in atomic spectroscopy, time-resolved measurements for quantum chemistry, nonlinear optics, and x-ray sources, with applications in health sciences and industrial machining [7]. For quantum light, energy-time entangled photons can also be produced with temporal features on ultrafast timescales [8–10] and the wide availability of pulsed lasers has made this regime accessible for quantum state engineering [11–13]. However, quantum interferometry with these states is challenging because the interference timescales are below the resolution of standard photon detectors [14,15]. To overcome detector limitations, optical techniques have been developed to directly observe energy-time entangled quantum states on ultrafast timescales [16,17] by building effective fast photon counters using ultrafast optical gating in conjunction with standard photon counters [18–20]. Extending the measurement of quantum interference to subpicosecond timescales will be essential for developing new applications with ultrafast energy-time states of light.

An important class of interferometers that has been used to observe quantum interference effects with energy-time entangled photons was developed by Franson in 1989 [21]. Photon pairs are sent through two unbalanced interferometers creating interference in the coincidence rate but not in the single-photon detection rates. High-visibility interference was observed in such an interferometer using spontaneous parametric downconversion (SPDC) [22,23]. Franson interferometers with energy-time entangled states have since become important for applications in long-distance quantum key distribution [24], measuring entanglement in high-dimensional [25] and multiphoton states [26,27], scaling quantum information tasks to larger dimensions [28,29], and improving molecular spectroscopy [30]. However, when both the single-photon and two-photon coherence times are ultrafast, as is often the case for SPDC photons produced with pulsed lasers, observing quantum interference effects with a Franson interferometer requires new techniques to overcome detector limitations and the original interferometer concept can be adapted to provide delays on shorter timescales.

In this work, we temporally resolve two-photon interference with subpicosecond timing resolution. The detectors are implemented by optically gating the photons in a nonlinear medium via noncollinear sum-frequency generation (SFG) with a short gate pulse [16,18–20]. Using this technique and single-photon spectrometers, we measure both the joint temporal and joint spectral features of a spatially separated two-photon state at the output of a Franson interferometer.

We produce energy-time entangled photon pairs with SPDC pumped by a broadband laser pulse. The photons are produced with strong anticorrelations between the signal ω_s and idler ω_i frequencies leading to a narrow joint uncertainty $\Delta(\omega_s + \omega_i)$ set by the bandwidth of the pump in broadly phase-matched materials [16,31]. For a two-photon state with no spectral phase, the photon pairs will also exhibit strong correlations between the time of arrival of the signal, t_s, and the idler, t_i, leading to smaller joint uncertainty than their individual widths in time, $\Delta(t_s - t_i) < \Delta t_{s,i}$ [16]. A Franson interferometer, shown schematically in Fig. 1(a), separates the photons on each side into a short and long path, with a time delay τ,

---

[*] jpmaclean@uwaterloo.ca
[†] john.matthew.donohue@upb.de

©2018 American Physical Society

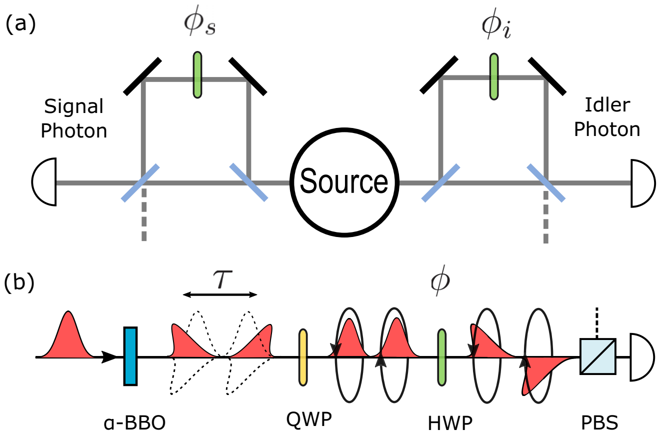

FIG. 1. Franson interferometer concept diagram. (a) Nonlocal interference can be seen by sending each photon of a two-photon energy-time entangled pair through an unbalanced interferometer. Each photon is split into early and late time bins and recombined with a phase applied to one bin. (b) In each arm of the Franson interferometer, the delays and phases are implemented through birefringent material and wave plates, creating a path difference on subpicosecond timescales between the short and long paths. A birefringent crystal (α-BBO) splits a horizontally polarized photon into a diagonal and a delayed antidiagonal mode. A quarter-wave plate (QWP) converts diagonal and antidiagonal to left- and right-circularly polarized light. A half-wave plate (HWP) introduces a phase between the circularly polarized photons. Both polarizations are then projected into the horizontal state with a polarizing beam splitter (PBS). See Appendix B for further details.

resulting in four possible combinations of paths. The single-photon detection rates, which vary with the phase in each arm, $\phi_{s,i}$, have a coherence time inversely proportional to the single-photon spectral bandwidth, $\tau_{c_{s,i}}^{(1)} = 1/\Delta\omega_{s,i}$, whereas the coincidence rate, which varies with $\phi_s + \phi_i$, has a two-photon coherence time inversely proportional to the two-photon spectral bandwidth, $\tau_c^{(2)} = 1/\Delta(\omega_s + \omega_i)$ (see Appendix D). When τ is set to be much larger than the single-photon coherence time but less than the two-photon coherence time, $\tau_{c_{s,i}}^{(1)} \ll \tau < \tau_c^{(2)}$, interference in the coincidence rate can be observed without any present in the single-detection rates.

The interference in the coincidences results from the indistinguishability between the cases where the two photons both take the short path in the interferometer and where both take the long path. Meanwhile, the cases where they take opposite paths, labeled short-long and long-short, do not exhibit interference, thus limiting the visibility to 50% without temporal resolution. This, however, is the same maximum visibility that can be obtained in coincidence measurements with classically correlated light when zero visibility is observed in the single-photon rates [32]. To observe higher visibility interference with energy-time entangled photons, sufficient time resolution is needed to resolve the arrival times of the early and late photons. This condition is typically met by using continuous-wave-pumped downconversion sources whose two-photon coherence times are much longer. They can therefore support interferometer delays in the range of 10 cm to 1 m [33–36], which can be implemented in free space or fiber, such that the time difference τ between early and late photons (30 μs to 3 ns) remains much larger than standard detector resolution.

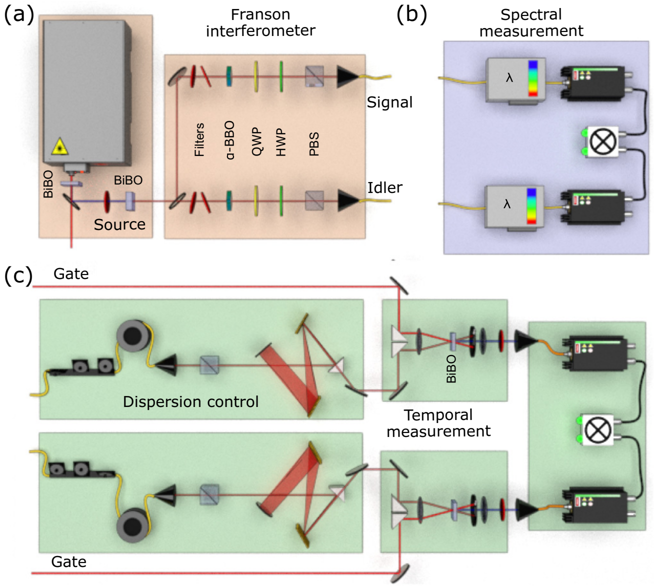

FIG. 2. Experimental setup. (a) A Ti:sapphire laser pulse [775 nm, 3.8 W average power, 0.120 ps (s.d.) pulse width], is frequency doubled in 2 mm of β-bismuth borate (BiBO). After spectral filtering with a 0.2 nm FHWM bandpass filter, the second harmonic [387.6 nm, 300 mW average power, approximately 0.940 ps (s.d.) coherence time] pumps a 5 mm BiBO crystal for type-I spontaneous parametric downconversion (SPDC) generating frequency entangled photons centered at 730 and 827 nm. The photons are separated by a dichroic mirror and their bandwidth is controlled by using tunable edge filters. Each photon passes through an unbalanced interferometer consisting of α-BBO, QWP, HWP, and PBS. We use 2.00 and 2.25 mm of α-BBO to create a difference between the short and long paths of $\tau_s = 0.820$ ps and $\tau_i = 0.910$ ps on the signal and idler side, respectively. The output of the Franson interferometer is coupled into single-mode fibers. (b) Spectral measurements are made with single-photon spectrometers. (c) Temporal measurements are made by using ultrafast gating with a strong laser pulse. A pair of grating compressors compensates for the dispersion introduced by the fibers.

We construct the ultrafast Franson interferometer by using birefringent crystals where the long and short paths arise due to the different refractive indices, and hence different optical path lengths, for horizontally and vertically polarized light [37], as seen in Fig. 1(b). Two millimeters of α-BBO creates an interferometer with relative delays below one picosecond and does not require any active phase stabilization. The experimental setup is shown in Fig. 2. Signal-idler photon pairs are produced by using SPDC with center wavelengths of 730 and 827 nm, respectively. A pair of tunable edge filters in the source control the single-photon spectral bandwidths by making effective bandpass filters of 3.0 nm (s.d.) and 3.5 nm, for the signal and idler, respectively. The photon pairs are coupled into the fiber, allowing for direct detection, spectral, or temporal measurements in coincidence, with or without the Franson interferometer. Spectral measurements are performed by using two grating-based single-photon monochromators with a resolution of approximately 0.1 nm, while temporal measurements are implemented by optically gating the

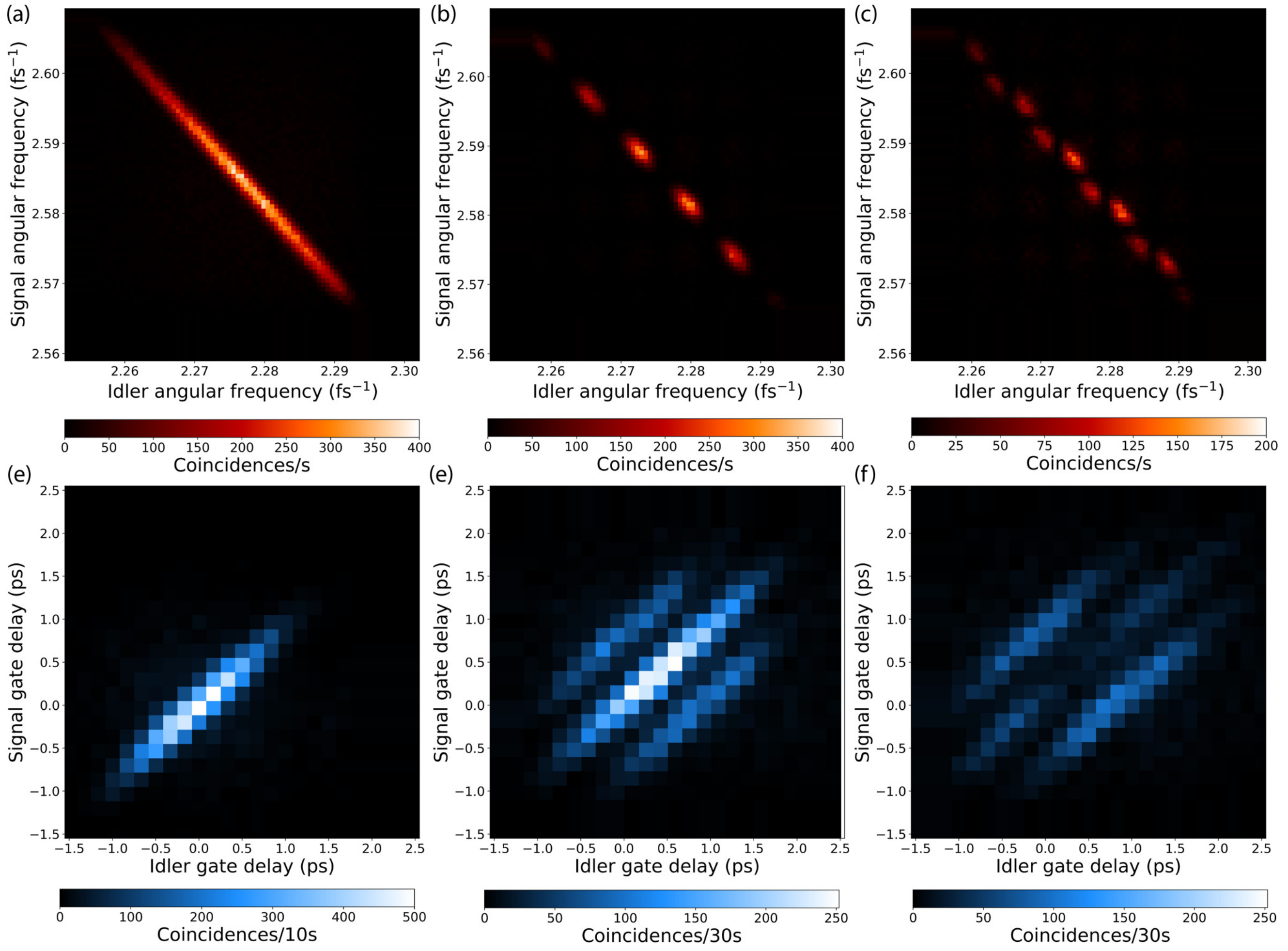

FIG. 3. The joint spectral intensity and joint temporal intensity of the two-photon state shown (a), (d) before and (b), (c), (e), (f) after the Franson interferometer. After the interferometer, different fringe patterns are observed in the joint spectrum for (b) constructive and (c) destructive interference. The interferometer shifts the temporal profile in (d) creating four different combinations of paths: short-short, short-long, long-short, and long-long. We observe (e) constructive and (f) destructive interference in the central peak between the cases where the photons both take the short path and both take the long path. These correspond to two-photon states where the signal and idler phases sum to (b), (e) $\phi_i + \phi_s = 0$, and (c), (f) $\phi_i + \phi_s = \pi$.

single-photons using SFG with femtosecond laser pulses which have an intensity pulse width of 0.120 ps (s.d.) [16].

The joint spectral intensity and joint temporal intensity of the state before the Franson interferometer were measured and the data are shown in Figs. 3(a) and 3(d), respectively. We observe strong anticorrelations between the photon frequencies and strong positive correlations between their arrival times. Measurements of the spectral widths in these plots allow us to estimate the one- and two-photon coherence times. To account for the finite resolution of the spectrometers and temporal gates, Gaussian fits to the measured widths are deconvolved assuming Gaussian response functions. The deconvolved frequency marginals (see Appendix A) are found to be $\Delta\omega_s = 10.65\ \mathrm{ps}^{-1}$ and $\Delta\omega_i = 9.57\ \mathrm{ps}^{-1}$, from which we estimate single-photon coherence times of $\tau_{c_s}^{(1)} = 0.094$ ps and $\tau_{c_i}^{(1)} = 0.105$ ps for the signal and idler, respectively. Gaussian fits to histograms of the spectral semiminor and semimajor axes yield deconvolved two-photon spectral bandwidths of $\Delta(\omega_s + \omega_i) = 1.531\ \mathrm{ps}^{-1}$ and $\Delta(\omega_s - \omega_i) = 17.81\ \mathrm{ps}^{-1}$. From the former, we estimate a two-photon coherence time of $\tau_c^{(2)} = 0.653$ ps. The temporal measurements yield deconvolved temporal marginal widths of $\Delta t_s = 0.455$ ps and $\Delta t_i = 0.488$ ps and deconvolved temporal widths of the semiminor and semimajor axes of $\Delta(t_s + t_i) = 0.895$ ps and $\Delta(t_s - t_i) = 0.091$ ps, respectively.

The joint spectral intensity and joint temporal intensity of the state *after* the Franson interferometer are shown in Figs. 3(b), 3(c), 3(e), and 3(f) for two different combinations of phase settings which provide the highest contrast between the constructive and destructive interference in the central peak of the temporal plots. In Fig. 3(b), we observe a joint spectral intensity similar to the one found in Fig. 3(a) but with a periodic amplitude modulation. The joint spectral intensity in Fig. 3(c) is also modulated by two sinusoidal functions, but shifted with respect to those in Fig. 3(b). These patterns correspond to the expected fringes for unbalanced interferometers applied to both the signal and idler, with phases $\phi_s + \phi_i = 0$ and $\phi_s + \phi_i = \pi$, respectively. In the corresponding temporal plots, we observe constructive interference in Fig. 3(e) and destructive interference in Fig. 3(f), presenting, respectively, a strong peak

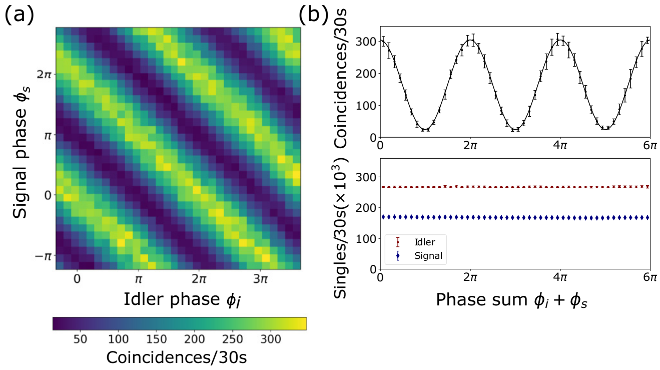

FIG. 4. Two-photon interference fringes. Franson interference between the upconverted signal and idler pair is measured by varying the signal and idler phases while setting the idler gate delay and signal gate delay halfway between the short and long paths of each side of the Franson interferometer. (a) We observe high-visibility interference with fringe oscillations along the diagonal which depend on the sum of the two phases $\phi_s + \phi_i$. (b) Weighted average of the coincidences and weighted average of the singles for the signal and idler pair as viewed as a function of their phase sum. Interference fringes display oscillations of $(85.3 \pm 0.4)\%$ visibility, while the singles detection events show no apparent oscillations.

and trough in the center of the distribution, while the two side peaks on either side of the central peak exhibit no interference. Through these measurements, we are able to observe the effect of the interferometer in both spectral and temporal domains.

We then measure the phase-dependent interference fringes of the Franson interferometer. The signal and idler gate delays are set to 0.455 and 0.410 ps, respectively, upconverting only the photons in the center of the joint temporal intensity where the highest contrast interference is observed, and corresponding to one pixel in Figs. 3(e) and 3(f). The measured coincidences as a function of the signal and idler phases, ϕ_s, ϕ_i, are presented in Fig. 4. We observe high-visibility interference fringes along one diagonal in Fig. 4(a), which corresponds to interference in the correlated phase setting, $\phi_s + \phi_i$, as expected for frequency anticorrelated photons (see Appendix E for further details). From the same data set, we plot the integrated single and coincidence rates as a function of the phase sum, $\phi_s + \phi_i$, in Fig. 4(b). The coincidence rate exhibits fringes with $(85.4 \pm 0.4)\%$ visibility without background subtraction, whereas the single-photon rates exhibit no visible interference. Error bars are obtained from a weighted average of the data points assuming Poissonian noise.

To maximize the visibility of the Franson interference, we found that the interferometer delays need to shift the joint-temporal intensity in Fig. 3(d) along its semimajor axis, such that a maximum overlap is obtained between the cases where both photons take the long path and where both photons take the short path. This can be achieved by matching the ratio of the applied interferometer delays τ to the ratio of the marginal temporal widths Δt, such that $\tau_i/\tau_s = \Delta t_i/\Delta t_s$. The measured ratio was $\Delta t_i/\Delta t_s = 1.07$, differing from unity due to the particular phase-matching conditions which can change the angle of the joint spectral amplitude function [38]. We found that using different lengths of α-BBO crystals, 2.00 and 2.25 mm, created the appropriate temporal separations of approximately $\tau_s = 0.820$ ps and $\tau_i = 0.910$ ps, for the signal and idler, respectively, in order to approach this ratio and satisfy the conditions for two-photon interference. We repeated the measurement when both crystal lengths were chosen to be 2.00 mm and observed a reduction of 10% in the visibility.

The measured detector counts for each phase setting on the signal and idler sides can be viewed as one binary outcome (+1) of a projective measurement, where the corresponding outcome (−1) is obtained by a π phase shift. Thus, we can look for a violation of the Clauser–Horne–Shimony–Holt (CHSH) inequality from 16 combinations of signal-idler phases, four outcomes for each of the four joint projective measurements in the inequality [24] (see Appendix C). We count for 200 s for each outcome and obtain from these counts a CHSH-Bell parameter of 2.42 ± 0.02, a violation of the local-hidden variable bound of two by 21 standard deviations [39]. This is a consequence of the entanglement in our system and shows the high quality of the interference and the general performance of our measurement device.

The visibility of the Franson interference and Bell violation could be further improved by reducing the second-harmonic generation (SHG) background from the laser in the optical gating. From the measured upconversion rates after the source, we obtain a coincidence rate of about 44 Hz from which about 0.8 Hz can be attributed to the SHG background of the laser. This corresponds to a signal-to-noise ratio (SNR) of 54. After the Franson interferometer, the measured coincidence rate at the peak is reduced by a factor of four but the SHG background remains the same, giving a SNR of 13.5. This translates to a reduction in visibility of 13%, which accounts for most of the observed visibility loss. The SHG background source could be reduced by utilizing a type-II process which would allow for additional polarization filtering.

We have experimentally observed two-photon quantum interference on ultrafast timescales. The optical gating detection mechanism enables the direct measurement of the joint temporal intensity as well as the observation of quantum interference phenomena and the violation of a CHSH-Bell inequality in a previously inaccessible regime. The Franson interferometer is stable and compact and could thus support future integration on chip. In addition to interferometry, access to both spectral and temporal features will provide new tools for creating and characterizing two-photon states and will be essential for new applications in quantum state engineering, such as shaping ultrafast entangled photon pulses.

The authors would like to thank M. Mazurek and K. Fisher for fruitful discussions. This research was supported in part by the Natural Sciences and Engineering Research Council of Canada (NSERC), Canada Research Chairs, Industry Canada, and the Canada Foundation for Innovation (CFI).

APPENDIX A: ADDITIONAL EXPERIMENTAL DETAILS

Photons from the source were detected at a rate of 626 000 coincidence counts per second with 3.6×10^6 and 3.3×10^6 single-detection events per second for the signal and idler, respectively. The heralded second-order coherence of the source, measured with a Hanbury Brown–Twiss interferometer, was $g^{(2)}(0) = 0.391 \pm 0.004$ for the signal and $g^{(2)}(0) = 0.395 \pm$

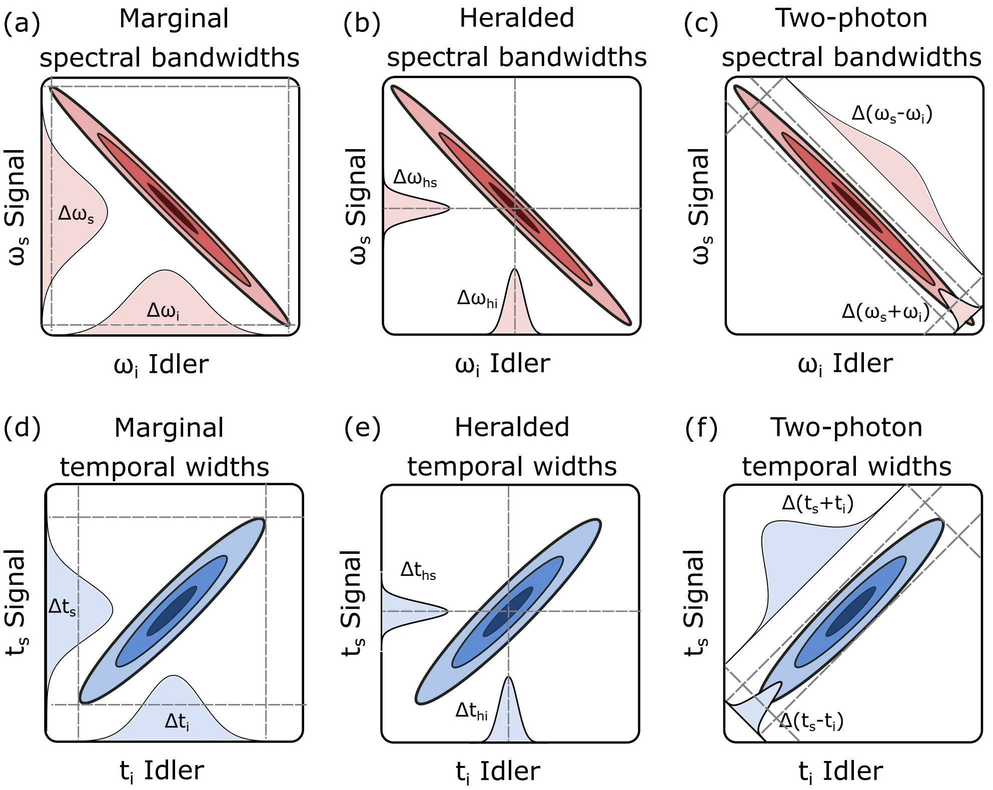
(a) Marginal spectral bandwidths
ωs Signal
ωi Idler
Δωs
Δωi
(b) Heralded spectral bandwidths
Δωhs
Δωhi
(c) Two-photon spectral bandwidths
Δ(ωs-ωi)
Δ(ωs+ωi)
(d) Marginal temporal widths
ts Signal
ti Idler
Δts
Δti
(e) Heralded temporal widths
Δths
Δthi
(f) Two-photon temporal widths
Δ(ts+ti)
Δ(ts-ti)

FIG. 5. Spectral bandwidths and temporal widths for a frequency anticorrelated two-photon SPDC state. (a) The single-photon spectral bandwidth $\Delta\omega$ is given by the marginal distribution obtained by projecting the joint spectral intensity onto either the signal or idler axes. The single-photon coherence time, the timescale over which interference in the single-photon rates can occur, is related to the inverse of the single-photon spectral bandwidth, $\tau_c^{(1)} = 1/\Delta\omega$. (b) The heralded spectral bandwidths $\Delta\omega_h$ are the spectral bandwidths of the signal or idler photon when the frequency of the other is fixed. (c) The two-photon spectral bandwidths for the semiminor, $\Delta(\omega_s + \omega_i)$, and semimajor axes, $\Delta(\omega_s - \omega_i)$, are obtained by projecting the joint spectral intensity along the corresponding diagonal axes $\omega_s \pm \omega_i$. The two-photon coherence time, the timescale over which interference in the coincidences can occur, is related to the inverse of the two-photon spectral bandwidth, $\tau_c^{(2)} = 1/\Delta(\omega_s + \omega_i)$. (d)–(f) The marginal temporal widths Δt, the heralded temporal widths Δt_h, as well as the two-photon temporal widths $\Delta(t_s \pm t_i)$ are obtained from the joint temporal intensity in the same way as their spectral analogs.

0.006 for the idler. In general, double-pair emission will lead to a broad background in the joint spectrum and joint temporal intensity; however, due to the tight temporal filtering on both sides, we estimate that double pairs contribute to less than 1% of the measured upconverted signal. After the upconversion on each side (without the Franson interferometer), approximately 44 coincidence counts (12 000 upconverted signal singles and 21 000 upconverted idler singles per second) per second were measured at the peak, from which about 0.8 coincidence counts (400 signal and 2500 idler singles) per second were background from the second harmonic of the gate pulse.

We present the fit parameters for the measured widths of the joint spectral intensity in Fig. 3(a) and the joint temporal intensity in Fig. 3(d) of the main text. The marginal widths are obtained by fitting the marginals of Figs. 3(a) and 3(d) to a one-dimensional Gaussian, while the heralded widths are obtained taking the average of several slices of the data when the frequency or time of one photon is fixed. A visual representation of the marginal and heralded widths is presented in Fig. 5. The statistical correlation, ρ, is obtained by finding the value that best fits a two-dimensional Gaussian with the measured marginals. The fit parameters are deconvolved assuming a Gaussian response function (see Supplemental Material of Ref. [16]), and these values are presented in parentheses alongside the values obtained from the raw measurements in Table I.

TABLE I. Fit parameters for the joint spectral intensity and the joint temporal intensity as seen in Figs. 3(a) and 3(d) of the main text. All measured values are standard deviations and values in parentheses are deconvolved from a Gaussian response function.

Property (deconvolved)		Joint spectrum	Joint-temporal intensity
Signal	Frequency (ω_0)	2584.6 ± 0.4 ps^{-1}	
	Marginal	10.65 ± 0.04 ps^{-1}	0.471 ± 0.004 ps
	width	(10.63 ± 0.04 ps^{-1})	(0.455 ± 0.004 ps)
	Heralded	1.25 ± 0.04 ps^{-1}	0.171 ± 0.009 ps
	width	(1.13 ± 0.05 ps^{-1})	(0.059 ± 0.022 ps)
Idler	Frequency (ω_0)	2276.7 ± 0.4 ps^{-1}	
	Marginal	9.57 ± 0.04 ps^{-1}	0.502 ± 0.005 ps
	width	(9.56 ± 0.04 ps^{-1})	(0.488 ± 0.005 ps)
	Heralded	1.13 ± 0.02 ps^{-1}	0.183 ± 0.010 ps
	width	(1.02 ± 0.02 ps^{-1})	(0.063 ± 0.023 ps)
	Statistical	-0.9929 ± 0.0001	0.920 ± 0.003
	correlation	(-0.9942 ± 0.0001)	(0.979 ± 0.004)

APPENDIX B: THE UNBALANCED INTERFEROMETER FOR ULTRAFAST PHOTONS

The experimental implementation of the Franson interferometer presented in Fig. 1 was chosen to provide a stable and compact method of creating time bin states with subpicosecond temporal separations. In this section, we analyze the transformations applied to the polarization state of the photon by the unbalanced interferometer in Fig. 1(b), composed of a birefringent crystal, wave plates, and a polarizing beam-splitter (PBS).

We denote the eigenstates of the Pauli operators σ_z as $|H\rangle$ and $|V\rangle$, representing the horizontal and vertical polarization states of light. After downconversion, the polarization state of each photon is vertical, $|\psi\rangle_{\text{pol}} = |V\rangle$. The α-barium borate (α-BBO) birefringent crystals at 45° separate the photons on each side into early $|e\rangle$ and late $|l\rangle$ time bins with a temporal separation of $\tau_s = 0.820$ ps and $\tau_i = 0.910$ ps, for the signal and idler, respectively. The two time bins have orthogonal polarizations, which we denote as diagonal, $|D\rangle = \frac{1}{\sqrt{2}}(|H\rangle + |V\rangle)$ and antidiagonal, $|A\rangle = \frac{1}{\sqrt{2}}(|H\rangle - |V\rangle)$. As a result, the polarization state is transformed to $|\psi\rangle_{\text{pol}} \rightarrow \frac{1}{\sqrt{2}}(|D\rangle|e\rangle + |A\rangle|l\rangle)$. The phase difference ϕ between the two time bins can be controlled by manipulating the polarization of the two modes after the α-BBO crystals with two wave plates and a PBS. A quarter-wave plate (QWP) first converts the two orthogonal polarization modes into left-circular $|L\rangle = \frac{1}{\sqrt{2}}(|H\rangle - i|V\rangle)$ and right-circular $|R\rangle = \frac{1}{\sqrt{2}}(|H\rangle + i|V\rangle)$ polarizations, resulting in the state $\frac{1}{\sqrt{2}}(|L\rangle|e\rangle + |R\rangle|l\rangle)$. A half-wave plate (HWP) at an angle θ, described by the unitary operator,

$$U_{\text{HWP}}(\theta) = i\begin{pmatrix} \cos 2\theta & \sin 2\theta \\ \sin 2\theta & -\cos 2\theta \end{pmatrix}, \tag{B1}$$

next applies the following transformations on the left- and right-circular polarizations of light,

$$U_{\text{HWP}}(\theta)|R\rangle = ie^{i2\theta}|L\rangle, \tag{B2}$$

$$U_{\text{HWP}}(\theta)|L\rangle = ie^{-i2\theta}|R\rangle, \tag{B3}$$

thus modifying the state to $\frac{1}{\sqrt{2}}i(e^{i2\theta}|R\rangle|e\rangle + e^{-i2\theta}|L\rangle|l\rangle)$. The PBS then erases the polarization information by projecting both circular polarizations into the horizontal mode $|H\rangle$, transforming the state to $\frac{1}{2}i|H\rangle(e^{-i2\theta}|e\rangle + e^{i2\theta}|l\rangle)$. As a result of these transformations, the photon at the output of the unbalanced interferometer is in a time-bin state with a phase difference between the early and late bins that can be set by the angle of the HWP through the parametrization $\phi = 4\theta$.

APPENDIX C: BELL INEQUALITY USING FRANSON INTERFEROMETRY

The measured detector counts for each phase setting ϕ in the unbalanced interferometers can be viewed as one binary outcome of a projective measurement, which we assign the value (+1). The corresponding outcome (−1) could be obtained by placing a second detector to measure the photon events at the second output port of the unbalanced interferometer; however, here the second outcome (−1) is instead obtained by measuring the photon events from the same detector but with an additional π phase shift introduced in the interferometer using the HWPs in Fig. 2. Given measurement outcomes ±1 for two measurement choices labeled a, a' for the signal and b, b' for the idler, we measure the coincidence rates for the four outcomes of each joint projective measurement, denoted $R_{i,j}(a,b)$, $(i,j = \pm 1)$, and evaluate the correlation coefficient [24],

TABLE II. Measured photon counts for CHSH-Bell inequality. The optical gate delays are set to upconvert photons in the center of the joint-temporal intensity. Upconverted coincidence counts are measured over 200 s for 16 combinations of signal-idler phases in the Franson interferometer. These correspond to projective measurements performed on the signal and idler sides, respectively labeled a, a' and b, b' with binary outcomes (±1) assigned for each phase setting.

				Signal phase (ϕ_s)			
				$7\pi/4$	$3\pi/4$	$\pi/4$	$5\pi/4$
				a		a'	
				(+1)	(−1)	(+1)	(−1)
Idler phase (ϕ_i)	0	b	(+1)	1292	367	1419	336
	π		(−1)	315	1331	329	1394
	$\pi/2$	b'	(+1)	1423	294	358	1333
	$3\pi/2$		(−1)	301	1469	1401	335

$$E(a,b) = \frac{R_{++}(a,b) + R_{--}(a,b) - R_{+-}(a,b) - R_{-+}(a,b)}{R_{++}(a,b) + R_{--}(a,b) + R_{+-}(a,b) + R_{-+}(a,b)}. \tag{C1}$$

Assuming a local-hidden variable model, the CHSH inequality [39] provides an upper limit to the combination of four correlation coefficients, which can be written as

$$S = |E(a,b) + E(a,b') + E(a',b) - E(a',b')| \leqslant 2. \tag{C2}$$

In Table II, we provide a table of raw coincidence counts for a particular combination of two projective measurements in the x-y plane of the time-bin Bloch sphere on both the signal and idler sides. From these counts, a CHSH-Bell parameter of $S = 2.42 \pm 0.02$ is obtained, thus violating the inequality by 21 standard deviations.

APPENDIX D: FRANSON INTERFEROMETRY WITH FINITE CORRELATIONS

In this section, we first calculate the overall coincident and single-photon detection rates of an energy-time entangled two-photon state after the Franson interferometer. We show that this leads to two distinct timescales of interference for the single-photon detection rates and the coincidence detection rate. We then describe the need for temporal selection to improve the visibility of the interference in the coincidence rate after the Franson interferometer and describe the effect of spectral or temporal selection by calculating the joint spectrum and joint temporal intensity for two-photon state after the Franson interferometer. Finally, we discuss the parameters for optimizing the visibility of the two-photon interference.

Consider the two-mode state with signal ω_s and idler ω_i frequency modes,

$$|\psi\rangle = \int d\omega_s d\omega_i F(\omega_s,\omega_i) a^\dagger_{\omega_s} a^\dagger_{\omega_i} |0\rangle. \tag{D1}$$

At the source, the joint spectral amplitude $F(\omega_s,\omega_i)$ of a pure two-mode state with no spectral phase can be described in Gaussian form as

$$F_{\text{source}}(\omega_s,\omega_i) = \frac{1}{\sqrt{2\pi\sigma_{\omega_s}\sigma_{\omega_i}}\left(1-\rho_\omega^2\right)^{1/4}} \exp\left(-\frac{1}{2\left(1-\rho_\omega^2\right)}\left[\frac{(\omega_s-\omega_{s0})^2}{2\sigma_{\omega_s}^2} + \frac{(\omega_i-\omega_{i0})^2}{2\sigma_{\omega_i}^2} - \frac{\rho_\omega(\omega_s-\omega_{s0})(\omega_i-\omega_{i0})}{\sigma_{\omega_s}\sigma_{\omega_i}}\right]\right), \tag{D2}$$

where σ_{ω_s} and σ_{ω_i} are the marginal bandwidths of the signal and idler, respectively, and where the correlation parameter $\rho_\omega = \Delta(\omega_s\omega_i)/\Delta\omega_s\Delta\omega_i$ describes the statistical correlations between the frequency of the signal and idler modes, and can be related to the purity of the partial trace, $P = (1-\rho_\omega^2)^{1/2}$. For frequency anticorrelated photons, as shown in Fig. 3(a), the frequency correlations are negative and $\rho_\omega < 0$.

The two paths (short and long) of each arm of the Franson interferometer are described by relative delays τ_s and τ_i along with phases ϕ_s and ϕ_i for the signal and idler, respectively. The joint spectral amplitude after the Franson interferometer takes the form

$$F_{\text{Franson}}(\omega_s,\omega_i) = F_{\text{source}}(\omega_s,\omega_i)\tfrac{1}{4}\left(1+e^{i(\omega_s\tau_s+\phi_s)}\right)\left(1+e^{i(\omega_i\tau_i+\phi_i)}\right). \tag{D3}$$

The overall coincidence rate directly after the interferometer is

$$\begin{aligned} C(\phi_s,\phi_i) &= \int_{-\infty}^{\infty} d\omega_s d\omega_i |F_{\text{Franson}}(\omega_s,\omega_i)|^2 \\ &\propto 1 + \exp\left(\frac{-\tau_s^2\sigma_{\omega_s}^2}{2}\right)\cos\left(\omega_{s0}\tau_s - \phi_s\right) + \exp\left(\frac{-\tau_i^2\sigma_{\omega_i}^2}{2}\right)\cos\left(\omega_{i0}\tau_i - \phi_i\right) \\ &\quad + \frac{1}{2}\exp\left[-\frac{1}{2}\left(\sigma_{\omega_s}\tau_s - \sigma_{\omega_i}\tau_i\right)^2 - (1+\rho_\omega)\sigma_{\omega_s}\sigma_{\omega_i}\tau_s\tau_i\right]\cos\left[(\omega_{s0}\tau_s-\phi_s)+(\omega_{i0}\tau_i-\phi_i)\right] \\ &\quad + \frac{1}{2}\exp\left[-\frac{1}{2}\left(\sigma_{\omega_s}\tau_s - \sigma_{\omega_i}\tau_i\right)^2 - (1-\rho_\omega)\sigma_{\omega_s}\sigma_{\omega_i}\tau_s\tau_i\right]\cos\left[(\omega_{s0}\tau_s-\phi_s)-(\omega_{i0}\tau_i-\phi_i)\right]. \end{aligned} \tag{D4}$$

For frequency anticorrelated photons, $\rho \to -1$, we expect interference which depends on the phase sum $\phi_s + \phi_i$, whereas for frequency correlated photons $\rho \to 1$, the interference depends on the phase difference $\phi_s - \phi_i$. Considering the idealized case of frequency anticorrelations ($\rho \to -1$), assuming the signal and idler photon bandwidths σ_ω are the same, and the interferometer delays τ are equal, Eq. (D4) simplifies to

$$\begin{aligned} C(\phi_s,\phi_i) &\propto 1 + \exp\left(\frac{-\tau^2\sigma_\omega^2}{2}\right)\cos\left(\omega_{s0}\tau - \phi_s\right) + \exp\left(\frac{-\tau^2\sigma_\omega^2}{2}\right)\cos\left(\omega_{i0}\tau - \phi_i\right) \\ &\quad + \frac{1}{2}\exp\left[-(1+\rho_\omega)\sigma_\omega^2\tau^2\right]\cos\left[(\omega_{s0}\tau-\phi_s)+(\omega_{i0}\tau-\phi_i)\right]. \end{aligned} \tag{D5}$$

On the other hand, single-photon detection events have interference fringes described by

$$S(\phi_j) \propto 1 + \exp\left(-\tfrac{1}{2}\sigma_{\omega_j}^2\tau_j^2\right)\cos\left(\omega_{j0}\tau_j - \phi_j\right), \tag{D6}$$

where $j \in \{s,i\}$. Comparing Eq. (D5) with Eq. (D6), we find there are two timescales for interference for the two-photon state from downconversion. The single-photon interference in Eq. (D6) varies with ϕ_j and has a coherence time that depends on the inverse bandwidth of the photons, $\tau_c^{(1)} = 1/\sigma_\omega = 1/\Delta\omega$, whereas the two-photon interference in Eq. (D5) varies with the sum $\phi_s + \phi_i$ and has a coherence time that depends on the two-photon spectral bandwidth, $\tau_c^{(2)} = 1/(\sqrt{2}\sqrt{1+\rho\sigma_\omega}) = 1/\Delta(\omega_s+\omega_i)$. The Franson interferometer can thus be used to separate these two timescales by setting the delay $1/\Delta\omega \ll \tau \leqslant 1/\Delta(\omega_s+\omega_i)$ between the single-photon and two-photon coherence times. Thus, with the appropriately chosen delay settings, we find that the singles detection rates are constant whereas the coincident detection rate has oscillating fringes which depend on $\phi_s + \phi_i$ with an interference visibility of $V = \frac{1}{2}\exp[-\frac{1}{2}\Delta(\omega_s+\omega_i)^2\tau^2]$. The visibility $V \leqslant \frac{1}{2}$ without temporal selection is limited by the noninterfering background contributions from the short-long and long-short paths of the interferometer. To improve the measured visibility, these noninterfering background terms must be temporally filtered.

APPENDIX E: FRANSON INTERFEROMETRY WITH SPECTRAL OR TEMPORAL SELECTION

We now discuss the spectral and temporal features of the downconverted state after the Franson interferometer. This is achieved by calculating the joint spectrum and joint temporal intensity. The joint spectrum is obtained from the modulus squared of Eq. (D3),

$$|F_{\text{Franson}}(\omega_s,\omega_i)|^2 = |F_{\text{source}}(\omega_s,\omega_i)|^2 \cos\left(\frac{\omega_{s0}\tau_s+\phi_s}{2}\right)^2 \times \cos\left(\frac{\omega_{i0}\tau_i+\phi_i}{2}\right)^2. \tag{E1}$$

It consists of the original source spectrum $|F_{\text{source}}(\omega_s,\omega_i)|^2$, which is intensity modulated. When $\phi_i+\phi_s=0$, the oscillations for the anticorrelated frequencies remain in phase, as in Fig. 3(b), whereas when $\phi_s+\phi_i=\pi$, they will be out of phase, as in Fig. 3(c).

The joint temporal amplitude is obtained by taking the Fourier transform of the joint spectral amplitude,

$$f_{\text{Franson}}(t_s,t_i) = \int d\omega_i d\omega_s F_{\text{Franson}}(\omega_i,\omega_s) e^{i\omega_i t_i} e^{i\omega_s t_s} \tag{E2}$$

from which we can obtain the joint temporal intensity,

$$\begin{aligned}
&|f_{\text{Franson}}(t_s,t_i)|^2\\
&\quad\propto f_{ss}^2(t_s,t_i)+f_{ls}^2(t_s,t_i)+f_{sl}^2(t_s,t_i)+f_{ll}^2(t_s,t_i)\\
&\qquad+2[f_{ss}(t_s,t_i)f_{ls}(t_s,t_i)+f_{sl}(t_s,t_i)f_{ll}(t_s,t_i)]\cos(\omega_{s0}\tau_s-\phi_s)\\
&\qquad+2[f_{ss}(t_s,t_i)f_{sl}(t_s,t_i)+f_{ls}(t_s,t_i)f_{ll}(t_s,t_i)]\cos(\omega_{i0}\tau_i-\phi_i)\\
&\qquad+2f_{sl}(t_s,t_i)f_{ls}(t_s,t_i)\cos[(\omega_{s0}\tau_s-\phi_s)-(\omega_{i0}\tau_i-\phi_i)]\\
&\qquad+2f_{ss}(t_s,t_i)f_{ll}(t_s,t_i)\cos[(\omega_{s0}\tau_s-\phi_s)+(\omega_{i0}\tau_i-\phi_i)],
\end{aligned} \tag{E3}$$

where

$$f_{ss}(t_s,t_i) = \exp[-(\sigma_{\omega_s}t_s-\sigma_{\omega_i}t_i)^2-2(1+\rho)\sigma_{\omega_s}\sigma_{\omega_i}t_st_i], \tag{E4}$$

$$\begin{aligned}f_{ls}(t_s,t_i) = \exp\{&-[\sigma_{\omega_s}(t_s+\tau_s)-\sigma_{\omega_i}t_i]^2\\ &-2(1+\rho)\sigma_{\omega_s}\sigma_{\omega_i}(t_s+\tau_s)t_i\},\end{aligned} \tag{E5}$$

$$\begin{aligned}f_{sl}(t_s,t_i) = \exp\{&-[\sigma_{\omega_s}t_s-\sigma_{\omega_i}(t_i+\tau_i)]^2\\ &-2(1+\rho)\sigma_{\omega_s}\sigma_{\omega_i}t_s(t_i+\tau_i)\},\end{aligned} \tag{E6}$$

$$\begin{aligned}f_{ll}(t_s,t_i) = \exp\{&-[\sigma_{\omega_s}(t_s+\tau_s)-\sigma_{\omega_i}(t_i+\tau_i)]^2\\ &-2(1+\rho)\sigma_{\omega_s}\sigma_{\omega_i}(t_s+\tau_s)(t_i+\tau_i)\},\end{aligned} \tag{E7}$$

are the four terms that represent the different combinations of paths the photons can take in the Franson interferometer, either short-short (f_{ss}), long-short (f_{ls}), short-long (f_{sl}), or long-long (f_{ll}). These are two-dimensional correlated Gaussian functions that are shifted with respect to the origin by the applied delays τ_i and τ_s. Different types of interference can occur between these paths. The first line in Eq. (E3) contains the noninterference terms, the second and third lines accounts for single-photon interference, while the fourth and fifth lines account for nonlocal two-photon interference, which depends on the overlap between f_{ls} and f_{sl} and between f_{ss} and f_{ll}, respectively. For anticorrelated photons ($\rho\to-1$), the short-long f_{sl} and long-short f_{ls} terms do not overlap and the fourth line goes to zero since $f_{sl}f_{ls}\to0$. The single-photon temporal marginal, on the other hand, is given by

$$\begin{aligned}|f_{\text{marginal}}(t)|^2 \propto{}& \exp[-2t^2(1-\rho_\omega{}^2)\sigma_\omega{}^2]+\exp[-2(t+\tau)^2(1-\rho_\omega{}^2)\sigma_\omega{}^2]\\ &+2\exp\left[-2t^2(1-\rho_\omega{}^2)\sigma_\omega{}^2\left(t+\frac{\tau}{2}\right)^2-\frac{1}{2}\sigma_\omega{}^2\tau_\omega{}^2\right]\cos(\tau\omega_0-\phi).\end{aligned} \tag{E8}$$

Comparing Eq. (E3) with Eq. (E8), we find, as before, two different timescales for two-photon and single-photon interference. The interference term which varies as $\phi_s+\phi_i$ depends on the overlap between f_{ss} and f_{ll}, whereas the single-photon interference has a coherence time that depends on the inverse bandwidth ($1/\sigma_\omega=1/\Delta\omega$) of the downconverted light.

To calculate the expected coincidence and single-photon rates with temporal selection, we consider the limiting case where we temporally select only the photon arrival times halfway between the short and long paths. This is equivalent to setting $t_s=-\tau_s/2$ and $t_i=-\tau_i/2$ in Eqs. (E3) and (E8), which simplify to

$$\begin{aligned}\left|f_{\text{Franson}}\left(-\frac{\tau_s}{2},-\frac{\tau_i}{2}\right)\right|^2 \propto{}& 2\exp\left(-\frac{1}{2}\sigma_{\omega_s}^2\tau_s^2-\frac{1}{2}\sigma_{\omega_i}^2\tau_i^2\right)[\cos(\omega_{s0}\tau_s-\phi_s)+\cos(\omega_{i0}\tau_i-\phi_i)]\\ &+\exp\left[-\frac{1}{2}(\sigma_{\omega_s}\tau_s-\sigma_{\omega_i}\tau_i)^2-(1+\rho_\omega)\sigma_{\omega_s}\sigma_{\omega_i}\tau_s\tau_i\right][1+\cos(\omega_{s0}\tau_s+\omega_{i0}\tau_i-\phi_s-\phi_i)],\end{aligned} \tag{E9}$$

$$\left|f_{\text{marginal}}\left(-\frac{\tau}{2}\right)\right|^2 \propto \exp\left[-\frac{1}{2}(1-\rho_\omega{}^2)\sigma_\omega{}^2\tau^2\right]+\exp\left(-\frac{1}{2}\sigma_\omega{}^2\tau^2\right)\cos(\omega_0\tau-\phi). \tag{E10}$$

The visibility of the two-photon interference term in Eq. (E9) is then maximized under two conditions: the ratio of the delays is proportional to the ratio of the marginal bandwidths, $\sigma_{\omega_s}\tau_s=\sigma_{\omega_i}\tau_i$, and the delays are less than the two-photon coherence time, $\tau_s\tau_i\ll1/[2(1+\rho)\sigma_{\omega_s}\sigma_{\omega_i}]$. Under these conditions, assuming the photon bandwidths are equal, and substituting the expressions for the single- and two-photon spectral bandwidths, the coincidence rate and single-photon rates of photon detections with temporal selection at $t_i=-\tau_i/2$ and $t_s=-\tau_s/2$ become

$$C(\phi_s,\phi_i) = \left|f_{\text{Franson}}\left(-\frac{\tau_s}{2},-\frac{\tau_i}{2}\right)\right|^2 \propto \exp\left[-\frac{1}{2}\Delta(\omega_s+\omega_i)^2\tau^2\right][1+\cos(\omega_{s0}\tau_s+\omega_{i0}\tau_i-\phi_s-\phi_i)], \tag{E11}$$

$$S(\phi_j) = \left|f_{\text{marginal}}\left(-\frac{\tau}{2}\right)\right|^2 \propto \exp\left[-\frac{1}{2}(1-\rho_\omega{}^2)\Delta\omega_j{}^2\tau^2\right]+\exp\left(-\frac{1}{2}\Delta\omega_j^2\tau^2\right)\cos(\omega_0\tau-\phi_j). \tag{E12}$$

As before, single-photon interference is removed by making the delays larger than the single-photon coherence time, $\tau \gg 1/\Delta\omega$. However. now, with temporal selection, the noninterfering terms have been filtered and 100% interference visibility can be achieved in the two-photon coincidence rate.

[1] S. Slussarenko, M. M. Weston, H. M. Chrzanowski, L. K. Shalm, V. B. Verma, S. W. Nam, and G. J. Pryde, Nat. Photonics **11**, 700 (2017).

[2] M. W. Mitchell, J. S. Lundeen, and A. M. Steinberg, Nature (London) **429**, 161 (2004).

[3] M. B. Nasr, B. E. A. Saleh, A. V. Sergienko, and M. C. Teich, Phys. Rev. Lett. **91**, 083601 (2003).

[4] A. M. Steinberg, P. G. Kwiat, and R. Y. Chiao, Phys. Rev. Lett. **68**, 2421 (1992).

[5] F. Kaiser, P. Vergyris, D. Aktas, C. Babin, L. Labonté, and S. Tanzilli, Light: Sci. Appl. **7**, 17163 (2018).

[6] J. Aasi *et al.*, Nat. Photonics **7**, 613 (2013).

[7] S. Backus, C. G. Durfee, M. M. Murnane, and H. C. Kapteyn, Rev. Sci. Instrum. **69**, 1207 (1998).

[8] B. Dayan, A. Pe'er, A. A. Friesem, and Y. Silberberg, Phys. Rev. Lett. **93**, 023005 (2004).

[9] M. B. Nasr, S. Carrasco, B. E. A. Saleh, A. V. Sergienko, M. C. Teich, J. P. Torres, L. Torner, D. S. Hum, and M. M. Fejer, Phys. Rev. Lett. **100**, 183601 (2008).

[10] S. Sensarn, G. Y. Yin, and S. E. Harris, Phys. Rev. Lett. **104**, 253602 (2010).

[11] W. P. Grice, A. B. U'Ren, and I. A. Walmsley, Phys. Rev. A **64**, 063815 (2001).

[12] P. J. Mosley, J. S. Lundeen, B. J. Smith, P. Wasylczyk, A. B. U'Ren, C. Silberhorn, and I. A. Walmsley, Phys. Rev. Lett. **100**, 133601 (2008).

[13] J. M. Donohue, M. Mastrovich, and K. J. Resch, Phys. Rev. Lett. **117**, 243602 (2016).

[14] R. H. Hadfield, Nat. Photonics **3**, 696 (2009).

[15] M. D. Eisaman, J. Fan, A. Migdall, and S. V. Polyakov, Rev. Sci. Instrum. **82**, 071101 (2011).

[16] J.-P. W. MacLean, J. M. Donohue, and K. J. Resch, Phys. Rev. Lett. **120**, 053601 (2018).

[17] R.-B. Jin, T. Saito, and R. Shimizu, arXiv:1801.09044.

[18] O. Kuzucu, F. N. Wong, S. Kurimura, and S. Tovstonog, Opt. Lett. **33**, 2257 (2008).

[19] O. Kuzucu, F. N. C. Wong, S. Kurimura, and S. Tovstonog, Phys. Rev. Lett. **101**, 153602 (2008).

[20] M. Allgaier, G. Vigh, V. Ansari, C. Eigner, V. Quiring, R. Ricken, B. Brecht, and C. Silberhorn, Quantum Sci. Technol. **2**, 034012 (2017).

[21] J. D. Franson, Phys. Rev. Lett. **62**, 2205 (1989).

[22] P. G. Kwiat, A. M. Steinberg, and R. Y. Chiao, Phys. Rev. A **47**, R2472 (1993).

[23] A. Pe'er, B. Dayan, A. A. Friesem, and Y. Silberberg, Phys. Rev. Lett. **94**, 073601 (2005).

[24] W. Tittel, J. Brendel, H. Zbinden, and N. Gisin, Phys. Rev. Lett. **81**, 3563 (1998).

[25] R. T. Thew, A. Acín, H. Zbinden, and N. Gisin, Phys. Rev. Lett. **93**, 010503 (2004).

[26] C. Reimer, M. Kues, P. Roztocki, B. Wetzel, F. Grazioso, B. E. Little, S. T. Chu, T. Johnston, Y. Bromberg, L. Caspani, D. J. Moss, and R. Morandotti, Science **351**, 1176 (2016).

[27] S. Agne, T. Kauten, J. Jin, E. Meyer-Scott, J. Z. Salvail, D. R. Hamel, K. J. Resch, G. Weihs, and T. Jennewein, Phys. Rev. Lett. **118**, 153602 (2017).

[28] T. Zhong, H. Zhou, R. D. Horansky, C. Lee, V. B. Verma, A. E. Lita, A. Restelli, J. C. Bienfang, R. P. Mirin, T. Gerrits, S. W. Nam, F. Marsili, M. D. Shaw, Z. Zhang, L. Wang, D. Englund, G. W. Wornell, J. H. Shapiro, and F. N. C. Wong, New J. Phys. **17**, 022002 (2015).

[29] T. Ikuta and H. Takesue, Sci. Rep. **8**, 817 (2018).

[30] M. G. Raymer, A. H. Marcus, J. R. Widom, and D. L. P. Vitullo, J. Phys. Chem. B **117**, 15559 (2013).

[31] Y. M. Mikhailova, P. A. Volkov, and M. V. Fedorov, Phys. Rev. A **78**, 062327 (2008).

[32] C. Su and K. Wódkiewicz, Phys. Rev. A **44**, 6097 (1991).

[33] J. Brendel, N. Gisin, W. Tittel, and H. Zbinden, Phys. Rev. Lett. **82**, 2594 (1999).

[34] D. Grassani, S. Azzini, M. Liscidini, M. Galli, M. J. Strain, M. Sorel, J. E. Sipe, and D. Bajoni, Optica **2**, 88 (2015).

[35] J. A. Jaramillo-Villegas, P. Imany, O. D. Odele, D. E. Leaird, Z.-Y. Ou, M. Qi, and A. M. Weiner, Optica **4**, 655 (2017).

[36] M. Peiris, K. Konthasinghe, and A. Muller, Phys. Rev. Lett. **118**, 030501 (2017).

[37] J. M. Donohue, M. Agnew, J. Lavoie, and K. J. Resch, Phys. Rev. Lett. **111**, 153602 (2013).

[38] W. P. Grice and I. A. Walmsley, Phys. Rev. A **56**, 1627 (1997).

[39] J. F. Clauser, M. A. Horne, A. Shimony, and R. A. Holt, Phys. Rev. Lett. **23**, 880 (1969).